Archie's Law in Sandy Microstructures

P. Mohammadmoradi, A. Kantzas
Department of Chemical and Petroleum Engineering, University of Calgary, Calgary, AB, Canada

Abstract

COMSOL Multiphysics® is used to directly simulate electric currents in pore-level unconsolidated and consolidated packings of spherical grains. The numerical workflows are applied to pore space geometries constructed by thousands of grains, covering a broad range of porosity and grain arrangements, to investigate the effects of geometrical parameters on the effective electrical conductivity of pore-level digital rocks. Predefined particle size distribution curves and porosities are used to reconstruct unconsolidated packings. A modified image dilation technique is applied to mimic the cementation process and consolidate the media. A pixel-wised pore morphological approach is utilized to predict the two-phase fluid occupancy profiles during drainage and imbibition at low capillary numbers. Stationary finite element simulations are then conducted in partially saturated microstructures to provide the electrical conductivity predictions. The post-processing results present the ad hoc parameters of Archie's law including tortuosity and formation factors, and cementation and saturation exponents. The conductivity plots highlight the significant role of wettability in shaping the electric current pathways and reveal the impacts of cementation, rock configuration, conductive phase saturation, and fluids spatial distributions on the flow of electric charges and petrophysical description of granular sandy microstructures.

Introduction

Determination of water/brine saturation is one of the most challenging and sensitive tasks of the petrophysical workflows as it helps to estimate the hydrocarbon saturation in underground petroleum reservoirs and construct field-scale saturation maps. This can be accomplished by interpretation of the resistivity well logs and application of the models relating fluid saturation to porosity, connate-water resistivity, and rock/fluid electrical properties. In this respect, Archie's law [1] is a well-known correlation relating the rock electrical conductivity to porosity and conductive phase saturation, where other fluids and rock grains are assumed as nonconductive phases. There are more sophisticated models as adaptations of the Archie equation that accommodate the effect of conductive solids such as shales on the rock electrical parameters.

The original Archie equation reads:

$$R_t = a\varphi^{-m}S_w^{-n}R_w \quad (1)$$

where R_t and φ denote the resistivity of partially saturated rock and rock porosity, respectively. R_w and S_w represent the resistivity and saturation of the conductive phase, which in sedimentary rocks is usually brine. a, m, and n are correlation constants known as tortuosity factor, cementation exponent, and saturation exponent, respectively. In this taxonomy, there are two important parameters called formation factor F and resistivity index I defined as:

$$F = \frac{a}{\varphi^m} \quad (2)$$

$$I = \frac{R_t}{R_o} = S_w^{-n} \quad (3)$$

where R_o denotes the resistivity of rock fully saturated by brine. Log-log plots of formation factor versus porosity help to find a and m as y-intercept and slope of the fitting line, respectively. Likewise, the slope of a best fit straight line to the resistivity index versus saturation data in a log-log graph denotes the saturation exponent. The cementation exponent explains the relationship between pore space geometry and resistivity which is a function of the rock tortuosity. As the hydraulic and electric tortuosities increase, the rock permeability diminishes and the cementation exponent increases [2]. The saturation exponent is a direct function of the non-conductive phase occupancy profile inside the pore-space. Therefore, it depends to the wettability of the rock and saturation history. For instance, in a strongly water-wet medium, the conductive wetting phase by filling the high capillarity zones and constructing a film over the grains keeps the rock conductive even at very small saturations. The tortuosity factor or lithology coefficient changes with compaction, pore structure, and grain size and lies in the range of 0.5 to 1.5. However, it is not necessarily an immediate representative of the electric or hydraulic tortuosity.

Governing Equations

A microscale domain represented by a binary digital image sequence is already discretized and prepared for numerical simulations [3,4]. COMSOL uses a finite-element method (FEM) to simulate the electrical currents under an imposed electric potential difference through the domain applying non-periodic boundary conditions. In this work, the "Electric Currents" module and the stationary solver are utilized

to predict the electrical conductivity and consequently the resistivity indices. The main governing equations are as follows:

$$\nabla . J = Q_j \quad (4)$$

$$J = \sigma E + J_e \quad (5)$$

$$E = -\nabla V \quad (6)$$

where σ, J and V denote electrical conductivity, current density, and electrical potential, respectively. By solving governing equations of the electric current with appropriate boundary conditions, the effective electrical conductivity is determined and then using **Eq.2** and **Eq.3** and the aforementioned log-log plots the Archie exponents are predicted [5]. The presumed electrical conductivity of brine is 1 S/m.

Pore Morphological Simulation

Two-phase drainage and imbibition displacements are simulated using a direct quasi-static pore morphological approach. The pore space of the binary three-dimensional images of porous media is characterized using expanding spheres. The pore size distribution is extracted; inlet and outlet faces are connected to sources and sinks; capillary dominant displacements are simulated applying some geometrical rules [6,7]. Bypassing and snap-off are responsible for trapping of the non-wetting phase during imbibition. There is no wetting phase trapping as the case studies are strongly wet and film flow provides thin depletion pathways. The capillary pressure is the only factor that dictates the fluid occupancy profiles throughout the pore space. The Young-Laplace equation as a nonlinear partial differential equation describes the capillary pressure equilibrium across the fluid-fluid interfaces. The Young–Laplace equation expresses the pressure difference as a function of surface tension, wettability, pore size, and shape of the interface. The model is acquired applying a normal stress balance over the interface as a surface of zero thickness:

$$P_c = \sigma \left(\frac{1}{r_1} - \frac{1}{r_2}\right) \quad (7)$$

where P_c and σ denote pressure difference across the interface and surface tension, respectively, and r_1 and r_2 are principal radii of the interface curvature.

Case Studies

Two different types of particle size distribution (PSD) curves with nonuniform (**A**) and uniform (**B**) grain sizes, borrowed from the McMurray formation description, are used to reconstruct four synthetic packing of grains applying the swelling spheres algorithm [8]. The **A2** and **B2** packings pose similar to **A1** and **B1**, respectively, having the same PSD curves, but additional grains and smaller porosities. The specifications of the case studies are listed in **Table.1**.

Table 1: Specifications of the case studies

Case	D_{50} (mm)	φ	No. of Grains	K (D)
A1	0.20	0.43	5000	56.51
A2	0.20	0.24	14081	5.135
B1	0.13	0.40	6261	15.59
B2	0.13	0.26	13042	2.783

Three-dimensional views of the case studies and samples of the predicted two-phase fluid occupancies during imbibition are depicted in **Fig.1-4**. The **A** samples contain small to large grains making the phase profiles and ganglia shapes more heterogeneous. Here, the surface tension is assumed equal to 30 mN/m and strongly oil-wet and strongly water-wet conditions are deployed as two extremes of wettability.

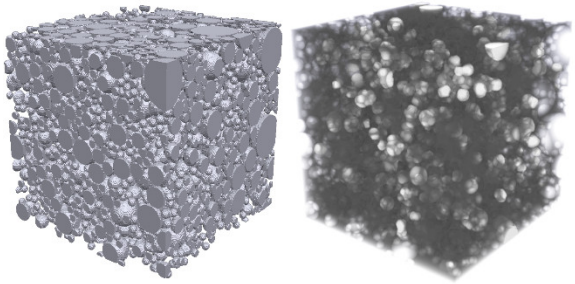

Figure 1. Three-dimensional renderings of **A1**, demonstrating the matrix (left) and a sample of the simulated two-phase fluid occupancies during imbibition (right); (gray, white, and transparent black colors represent solid, nonwetting, and wetting phases, respectively).

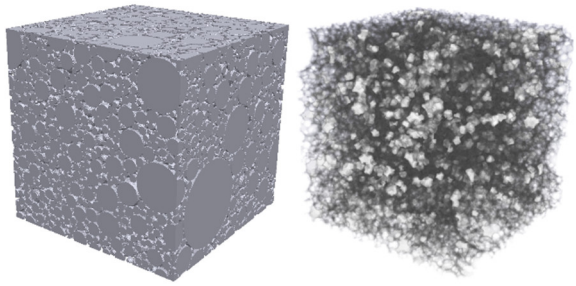

Figure 2. Three-dimensional renderings of **A2**, demonstrating the matrix (left) and a sample of the simulated two-phase fluid occupancies during imbibition (right); (gray, white, and transparent black colors represent solid, nonwetting, and wetting phases, respectively).

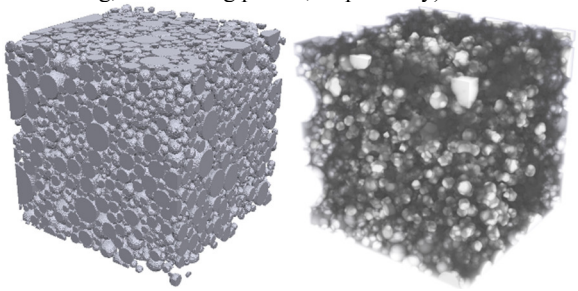

Figure 3. Three-dimensional renderings of **B1**, demonstrating the matrix (left) and a sample of the simulated two-phase fluid occupancies during imbibition (right); (gray, white, and transparent black colors represent solid, nonwetting, and wetting phases, respectively).

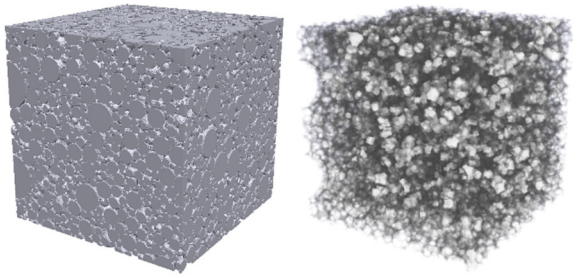

Figure 4. Three-dimensional renderings of **B2**, demonstrating the matrix (left) and a sample of the simulated two-phase fluid occupancies during imbibition (right); (gray, white, and transparent black colors represent solid, nonwetting, and wetting phases, respectively).

Simulation Results

In water-wet conditions, during drainage, the nonwetting phase invades pore space starting from low capillarity zones and during imbibition, brine might either fill the larger pores in the last stages or just bypass them as residual ganglia. Therefore, the main elements contributing to the electrical flows are the small and intermediate pores. In oil-wet conditions, brine only has access to intermediate-to-large pores and by dropping the pressure soon loses its connections to the inlet and outlet faces. This is well presented in **Fig.5** as a two-dimensional illustration of fluid distribution within **A1** under water-wet and oil-wet conditions at a brine saturation of 19 percent.

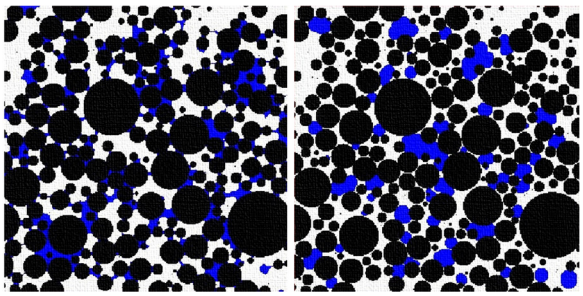

Figure 5. Demonstration of the predicted brine distribution at 19 percent saturation in two water-wet (left) and oil-wet (right) wetting conditions (black and blue colors represent solid and brine, respectively).

The simulated two-phase maps provide the computational domains for steady-state FEM simulations. However, the pressure-wised nature of the pore morphological simulations leads to limited/inadequate number of realizations, particularly at low brine saturations. The occupancy maps of brine, as the only conductive phase, are fed into COMSOL Multiphysics, the appropriate boundary condition is applied, and the electrical conductivity and consequently formation factor, resistivity index, and electric tortuosities are calculated. **Fig.6** represents the imposed electric potential surfaces in **A2** and **Fig.7-10** demonstrate the simulated electrical current streamlines through the case studies.

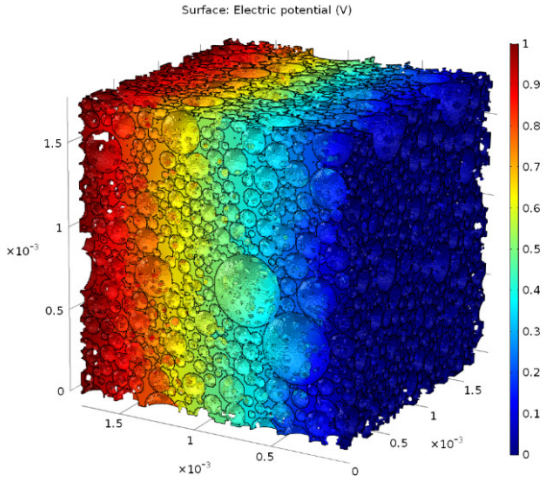

Figure 6. Three-dimensional demonstration of the applied electric potential through **A2** for prediction of electrical conductivity.

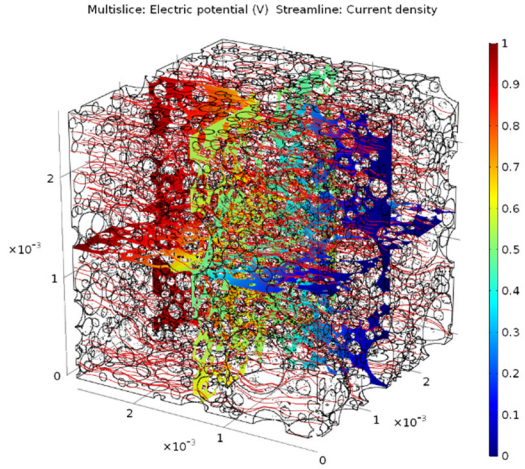

Figure 7. Three-dimensional representation of the applied electric potential and the predicted current streamlines during the electrical simulations through **A1**. (τ_e=1.11)

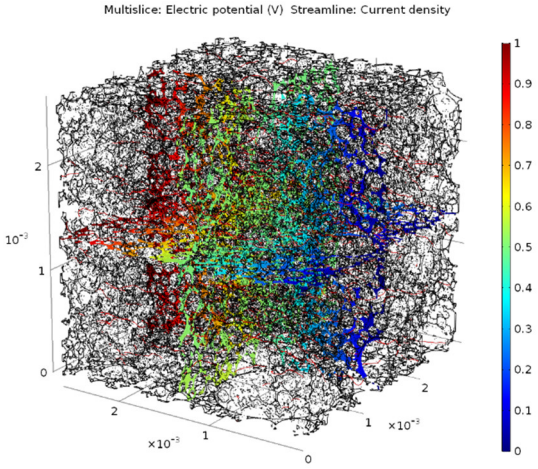

Figure 8. Three-dimensional representation of the applied electric potential and the predicted current streamlines during the electrical simulations through **A2**. (τ_e=1.18)

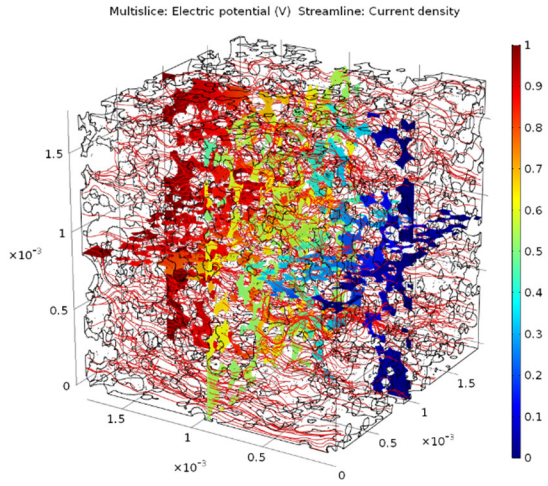

Figure 9. Three-dimensional representation of the applied electric potential and the predicted current streamlines during the electrical simulations through **B1**. (τ_e=1.13)

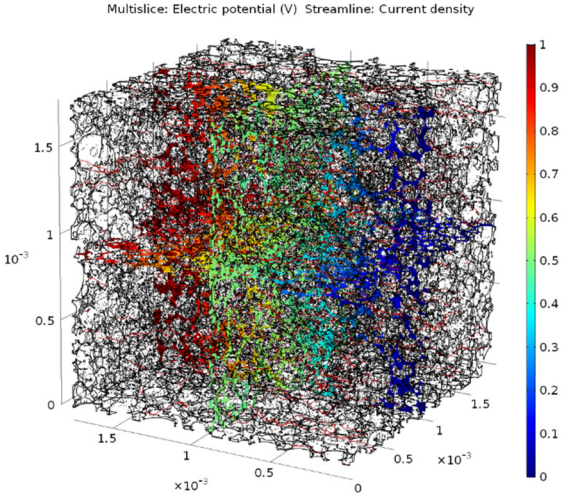

Figure 10. Three-dimensional representation of the applied electric potential and the predicted current streamlines during the electrical simulations through **B2**. (τ_e=1.17)

The streamlines within the high porosity samples are straighter leading to a higher electrical conductivity. In the following sections, the results of the FEM simulations are presented in graphs, and the effects of wettability, saturation history, and cementation on Archie exponents will be discussed.

Effect of rock porosity

Fig.11 shows the calculated formation factor versus porosity for **A** and **B** unconsolidated samples in a log-log plot. According to the best line crossing all data points, the tortuosity factor and cementation exponent are equal to 1.09 and 1.38, respectively. Formation factor calculations are conducted on fully saturated media. To predict the saturation exponents, two-phase drainage and imbibition process are simulated, and then electrical simulations are carried out through the brine profiles. **Fig.12-13** represent the obtained values of the resistivity index versus brine saturation. The saturation exponents of the **B** samples are slightly higher than **A** media, and there is a minor difference between the saturation exponents within each cluster. Small values of saturation exponents (<2) and resistivity indices might be sourced from the unconsolidated nature of the case studies.

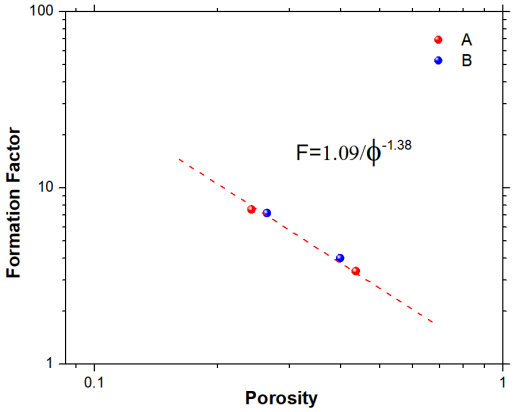

Figure 11. Predicted formation factor versus porosity for all case studies.

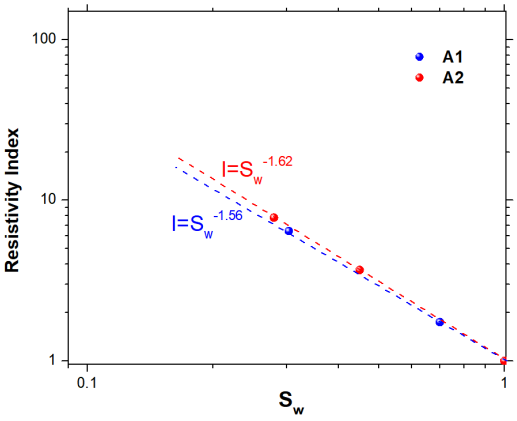

Figure 12. Predicted resistivity index versus water saturation and the saturation exponents for **A** samples.

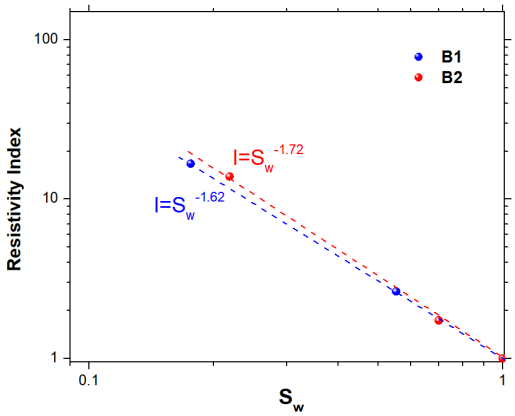

Figure 13. Predicted resistivity index versus water saturation and the saturation exponents for **B** samples.

Effect of rock wettability

According to the experimental measurements, there is a linear relationship between wettability and saturation exponent [9, 10] and the slope of the line appears to be a function of the petrophysical characteristics of the medium. In water-wet systems, the saturation exponent is smaller than 2, for mixed-wet systems is in order of 2 to 3, and much higher values (~3-5) happen in oil-wet systems [11]. Here, similar results are acquired, and as the wettability changes from water-wet to oil-wet, the saturation exponent increases from ~1.7 to ~3.4, **Fig.14-17**. As discussed and showed in **Fig.5,** the higher saturation exponents in oil-wet systems can be explained by consideration of the connectivity of brine. The non-conductive phase remains well connected throughout the pore space even at low saturations, while brine is poorly connected except at relatively high saturations.

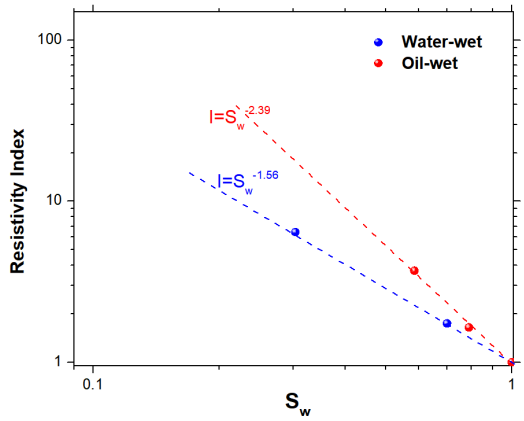

Figure 14. Predicted resistivity index versus water saturation and the saturation exponents of **A1** in water-wet and oil-wet conditions.

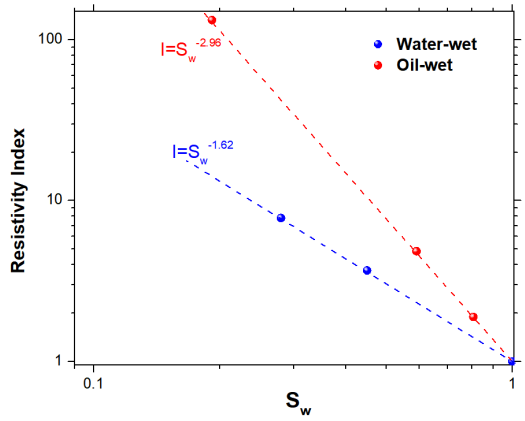

Figure 15. Predicted resistivity index versus water saturation and the saturation exponents of **A2** in water-wet and oil-wet conditions.

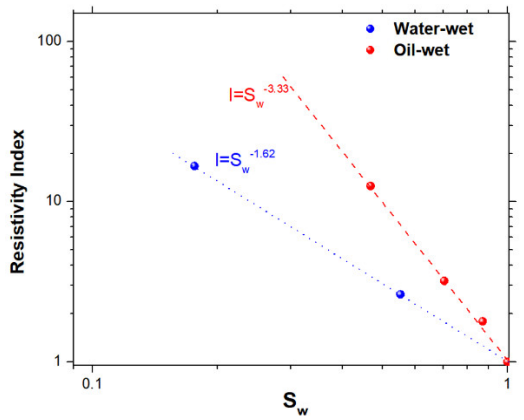

Figure 16. Predicted resistivity index versus water saturation and the saturation exponents of **B1** in water-wet and oil-wet conditions.

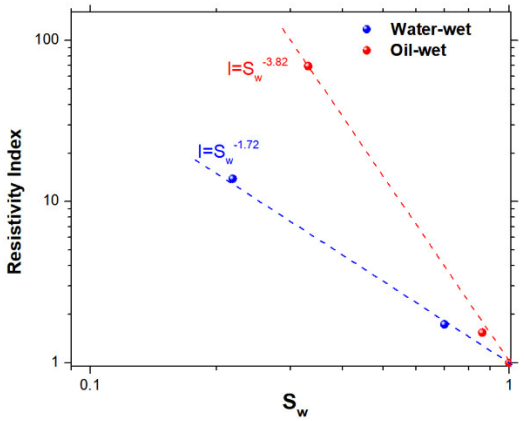

Figure 17. Predicted resistivity index versus water saturation and the saturation exponents of **B2** in water-wet and oil-wet conditions.

Effect of saturation history

The resistivity index appears sensitive to the spatial occupancy profile of the non-conducting fluid, and consequently, it is influenced by the wettability and saturation history [12]. **Fig.18-21** illustrate the resistivity index plots for drainage and imbibition in both water-wet and oil-wet conditions. The worst-case scenario for electrical conductivity happens during oil imbibition into an oil-wet medium. In a water-wet medium, there is a decrease in saturation exponents as the displacement scenario changes from drainage to imbibition. Although the type of pore-level displacements alters the Archie exponents, the effect of wettability alteration on the saturation exponents seems more noteworthy than the saturation history. Similar hysteresis effects on resistivity index has been observed in previous experimental studies [13].

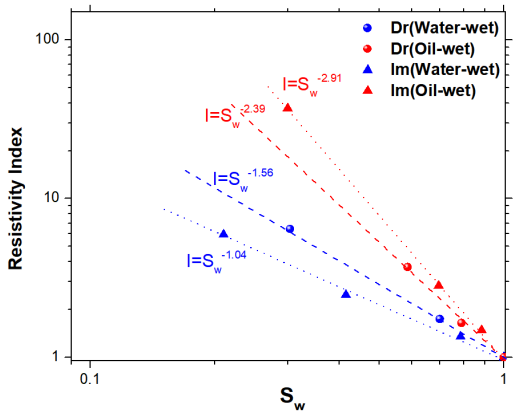

Figure 18. Predicted resistivity index versus water saturation and the saturation exponents of **A1** in water-wet and oil-wet conditions during drainage and imbibition.

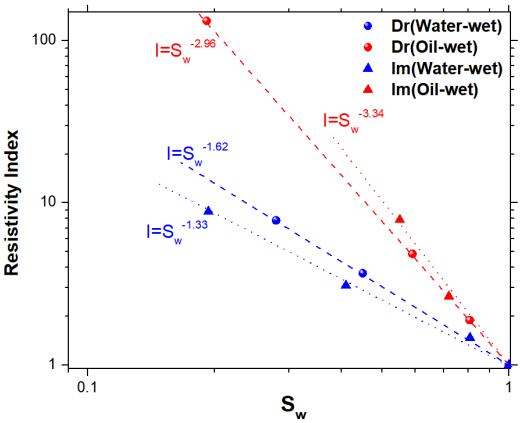

Figure 19. Predicted resistivity index versus water saturation and the saturation exponents of **A2** in water-wet and oil-wet conditions during drainage and imbibition.

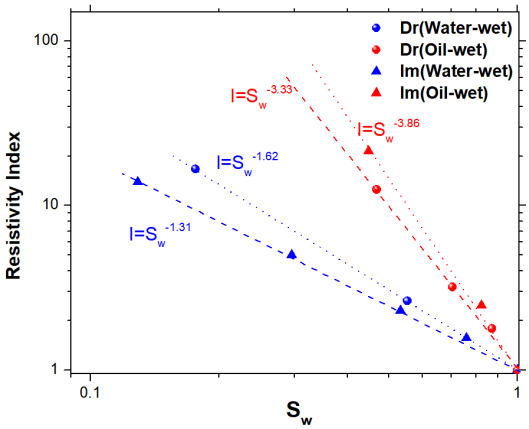

Figure 20. Predicted resistivity index versus water saturation and the saturation exponents of **B1** in water-wet and oil-wet conditions during drainage and imbibition.

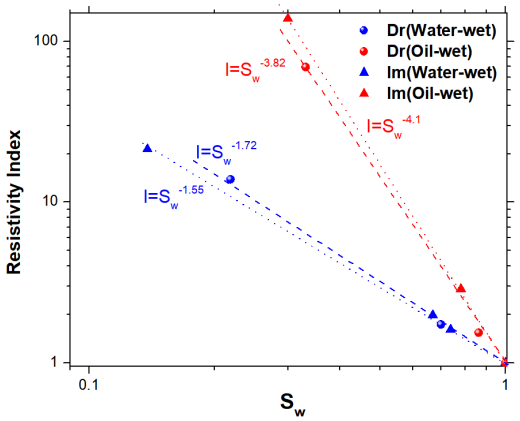

Figure 21. Predicted resistivity index versus water saturation and the saturation exponents of **B2** in water-wet and oil-wet conditions during drainage and imbibition.

Effect of Cementation

The cementation exponent has been reported around 1.3 for unconsolidated sands and is expected to increase with cementation [14]. Here, a modified image dilation technique is used to introduce cement into the narrow space between the grains and mimic the cementation process, **Fig.22**. By adding 11 percent PV cement to the original media, the formation factor of **A1**, **A2**, **B1**, and **B2** increases by 20, 29, 32, and 37 percent, respectively. The tortuosity factor and cementation exponent increase from 1.09 and 1.34 to 1.24 and 1.5, respectively. As depicted in **Fig.23**, filling 11 percent of **A1** pore space with cement has a marginal effect on its saturation exponent.

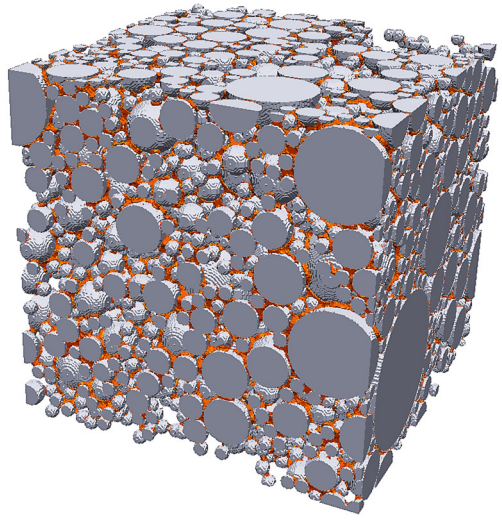

Figure 22. Three-dimensional demonstration of the introduced cement to consolidate grains of **A1** using image dilation technique. (orange and gray colors represent cement and matrix, respectively).

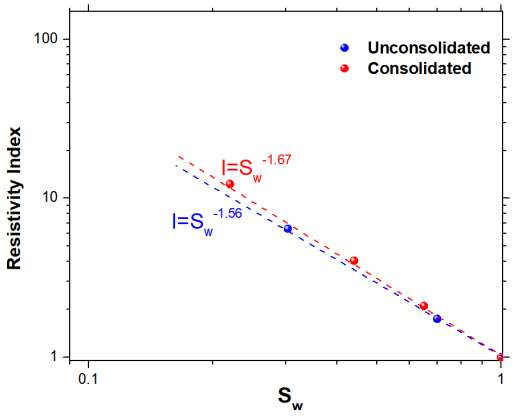

Figure 23. Predicted resistivity index versus water saturation and the saturation exponents of **A1** before and after the cementation process.

Conclusions

Conventional log interpretation models are ambiguous in providing an explanation for the relationship between rock resistivity and rock and pore space structure, fluid occupancies, wettability, and saturation history. The evolving digital rock physics models can revolutionize the petrophysical characterization workflows in the near future. In this paper, the potential of applying the image reconstruction and processing techniques together with FEM simulations in providing petrophysical interpretations was demonstrated. Numerical simulations were conducted on four consolidated, and unconsolidated packings of spherical grains and the key findings are as follows:

- In unconsolidated packings, rock configuration and porosity show a negligible effect on the saturation exponent.
- Wettability is the primary factor controlling the fluids distribution and therefore remarkably influences the saturation exponent.
- Saturation history slightly affects the saturation exponent. In comparison with drainage saturation exponents, imbibition exponents in oil-wet and water-wet conditions are higher and lower, respectively.
- The cementation exponent increases with medium consolidation, and more pronounced variations occur for packings with uniform grains.

References

1. Archie, G. E., 1952, Classification of carbonate reservoir rocks and petrophysical considerations: AAPG Bulletin, vol. 36, no. 2, p. 218–298.
2. Goudarzi, B., Mohammadmoradi, P., Kantzas, A. (2017). Direct Pore-level Examination of Hydraulic-Electric Analogy in Porous Media, SPE Offshore Technology Conference, OTC-28095-MS.
3. Mohammadmoradi, P., Kantzas, A. (2016). Pore Scale Investigation of Wettability Effect on Waterflood Performance. Society of Petroleum Engineers. doi:10.2118/181309-MS.
4. Knackstedt, M. A., Arns, C. H., Sheppard, A. P., Senden, T. J., Sok, R. M., Cinar, Y. Padhy, G. S. (2007). Archie's exponents in complex lithologies derived from 3D digital core analysis. Society of Petrophysicists and Well-Log Analysts.
5. Mohammadmoradi, P., Behrang, A., Taheri, S., Kantzas, A. (2017). Thermal conductivity of partially saturated microstructures. International Journal of Thermal Sciences, 112, 289-303.
6. Mohammadmoradi, P., Taheri, S., Kantzas, A. (2017). Interfacial Areas in Athabasca Oil Sands. Energy & Fuels.
7. Mohammadmoradi, P., Kantzas, A. (2016) Pore-Level Bénard–Marangoni Convection in Microgravity. COMSOL 2016, Boston, USA.
8. Taheri, S., Ghomeshi, S., & Kantzas, A. (2017). Permeability calculations in unconsolidated homogeneous sands. Powder Technology.
9. Donaldson, E. C., Siddiqui, T. K. (1989). Relationship Between the Archie Saturation Exponent and Wettability. Society of Petroleum Engineers. doi:10.2118/16790-PA
10. Morgan, W. B., Pirson, S. J. (1964). The effect of fractional wettability on the Archie saturation exponent. SPWLA 5th Annual Logging Symposium.
11. Abdassah, D., Permadi, P., Sumantri, Y., Sumantri, R. (1998). Saturation exponent at various wetting condition: fractal modeling of thin-sections. Journal of Petroleum Science and Engineering, 20(3), 147-154.
12. Stalheim, S. O., Eidesmo, T. (1995). Is The Saturation Exponent a Constant? Society of Petrophysicists and Well-Log Analysts.
13. Tweheyo, M. T., Talukdar, M. S., Torsæter, O. (2001). Hysteresis effects in capillary pressure, relative permeability and resistivity index of north sea chalk. In Paper SCA 2001-65 presented at the International Symposium of the Society of Core Analysts held in Edinburgh, UK.
14. Verwer, K., Eberli, G. P., Weger, R. J. (2011). Effect of pore structure on electrical resistivity in carbonates. AAPG bulletin, 95(2), 175-190.

Acknowledgements

The authors gratefully acknowledge the financial support of the FUR program from NSERC, AITF, and the sponsoring companies: Athabasca Oil Corporation, Devon Canada, Foundation CMG, Husky Energy, Brion Energy, Canadian Natural, Maersk Oil, Suncor Energy, and Schulich School of Engineering (University of Calgary).